Analytical model of the dynamic behavior of a vibrating mesh nebulizer for optimal atomization efficiency

P. Fossat, Mohamed Ichchou, Olivier Bareille

Version of Record: https://www.sciencedirect.com/science/article/pii/S0924424722002849
Manuscript_dc11d07b7295635a0cc240db48fb2bf5

Analytical model of the dynamic behavior of a vibrating mesh nebulizer for optimal atomization efficiency

Pascal Fossat[a,*], Mohamed Ichchou[a], Olivier Bareille[a]

[a] *Vibroacoustics and Complex Media Research Group VIAME, LTDS - CNRS UMR 5513, Centre Lyonnais d'Acoustique CeLyA, École Centrale de Lyon, Université de Lyon, France*

Abstract

This work deals with the assessment of optimal working condition of a mesh nebulizer on-demand droplet generation. The purpose of this paper is to introduce a model of vibrating mesh nebulizer to identify optimal working regime from a mechanical point of view. The influence of geometrical parameters and mechanical properties of both the piezoelectric component, vibrating plate and geometry of perforations is investigated and discussed based on an analytical model of stepped plate. This model is validated by 2D-axisymmetric finite element computations. The main trends identified by the model are recovered by the simulation and enable to formulate design rules to maximize the atomization efficiency with respect to a given set of mechanical and geometrical parameters.

Keywords: Ultrasonic atomization, Piezoelectric actuator, Vibrating mesh nebulizer, Perforated plate

*Corresponding author
Email address: pascal.fossat@ec-lyon.fr (Pascal Fossat)

Highlights

- Atomization efficiency depends on amount of fluid set in motion above the vibrating mesh and volume variation in apertures,
- Analytical model describes the pumping effect according to the position of holes and shape, and distribution over the plate,
- Design rules are suggested to take advantage of kinematics of both vibrating mesh and piezoelectric ring to increase volume variation,
- Successive finite element validations of theoretical results confirm relevancy of the model.

Introduction

Atomizers for on-demand droplet generation are usually classified into three main categories : air-jet, ultrasonic, and vibrating mesh nebulizers. Air-jet nebulizers (pneumatic nebulizers) atomize the liquid into droplets using a compressed gas traveling through a convergent nozzle. In ultrasonic nebulizers, high frequency acoustic waves are produced by a piezoelectric crystal as an energy source to overcome the capillary stress stabilizing the liquid surface and therefore breaking it into microsized droplets [1]. Vibrating mesh nebulizers are themselves divided in two categories. In passive devices, the liquid to be atomized is in between a vibrating piezoelectric patch and a fixed perforated mesh having identical tapered holes. As the piezoelectric crystal is driven by a high-frequency vibration, it pushes the fluid through the apertures of the perforated mesh [2]. Active vibrating mesh devices consist in a piezoelectric ring clamped on the contour of a perforated plate, as depicted in Fig. 1. When a voltage is applied to the piezoelectric ring, the disc contracts and expands, resulting in a transverse vibration of the perforated plate, and therefore pumping the fluid from one face of the mesh to the other one, resulting in droplet ejection [3].

Vibrating mesh nebulizers have several advantages compared to jet nebulizers including quiet operation, no heating, stability, low weight, fast response and energy efficiency. A decisive advantage is to control the droplet size by the ultrasonic frequency unlike jet nebulizers. Such vibrating mesh nebulizers utilize a membrane with multiple apertures and are reported to provide a more uniform droplet size. The only limitation is that these are manufactured through an expensive laser drilling process or micro- electroplating method. Despite the manufacturing costs, vibrating mesh nebulizers have been introduced in the 1980s for medical purposes. These devices are now used in various fields of application such as medicine, injection engines, agriculture, for various purposes such as disinfection, spray drying, atomization of liquids or powders [5, 6].

Regarding the actuation of vibrating mesh nebulizers, the key component is a plate that is perforated with precisely formed (tapered/cylindrical) holes. A piezoelectric ring clamped on the contour of the plate is driven by a electric excitation so that it vibrations induces downward and upward motion of the plate. The mesh deforms into the liquid side, thus pumping and loading the liquid inside holes. This deformation on the other side of the liquid reservoir ejects droplet through the holes. The specific motion of the apertures of the

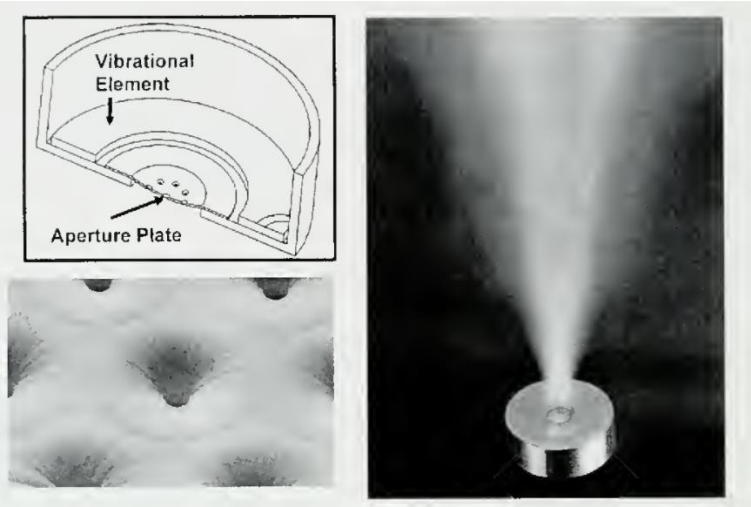

Figure 1: Constituents of a vibrating mesh nebulizer. Top left: the piezoelectric ring is actuated to expand and contract and induces local vibrations of the perforated plate that creates a pumping action. Bottom left: Microscopic view of perforations. There are approximately 1.000 holes on the perforated mesh. Right: mist resulting from atomization process. Picture taken from [4]

mesh creates a pumping effect that brings the liquid through the apertures so that it is finally atomized into fine droplets. The specific mechanism of droplet formation and ejection is not addressed in this paper. It is a complex multi-parameter two-phase flow problem and numerous competing theories are available in the literature [7, 8].

The huge interest in controlling accurately the size of these droplets and make sure the atomizer consistently generates droplets in a fine range of diameters has motivated numerous experimental studies. These concluded that the size of the droplet produced depends on the diameter of the holes in the mesh and physico-chemical properties of the liquid to be atomized, such as density, surface tension, and viscosity. The typical output droplet diameter is about 5 µm [9]. This size of particle is associated with deep lung penetration and explains the huge amount of experimental studies applied to drug delivery.

However, only a few research are available on the dynamic characteristics

and the underlying mechanism of mechanical vibration of the piezo and the perforated plate.

Among the very few works available from the mechanical perspective, one may cite [10] who concluded that the second vibration mode of the inner mesh provides more stable atomization efficiency and that the nodal line of the second mode should be inside the inner radius of the piezoelectric ring. Analytical solutions for the deflection of the plate actuated by a piezoelectric annular plate is fully documented in terms of efforts and moments in [11] and [12] but it resulted in static solutions only with no effect of the perforations. An investigation of the behavior of a piezo ring was suggested by [13] and demonstrated the effect of laminate's thickness, annular radius, and residual stresses on the deflection of the inner plate. An analytical model assessing the pumping effect caused by the perforated mesh was introduced in [14]. The cone angle was correlated to the flow resistance coefficient and pressure loss calculation, but it was not investigated in the frequency domain. This was later verified experimentaly in [15, 16, 17]. Recently, a modal study of the piezoelectric ring coupled with the plate was achieved by [18, 19] and was correlated to flow rates to demonstrate a better efficiency at the resonance frequency, but no investigation of the holes was conducted. More recently, a vibration-based model for annular-type bimorph transducers was published by [20]. The relationships between the transducer, its boundary conditions, and their influence on ultrasonic drying enabled to optimize the dryer design based on modal considerations.

From this critical review, and despite dozens of patents on the topic, published data on the design rules of these actuators are quite limited. Thus, the main purpose of the present paper is to investigate the features of a vibrating mesh nebulizer from the mechanical perspective.

The structure under study is described in section 1, the underlying physics and associated mechanisms. A simple analytical model is firstly derived in section 2 to evaluate the volume change of fluid that is set in motion by the plate and evaluate how it is affected by the plate's properties. A more specific model describing the volume variation in the mesh is then suggested in section 3 to investigate the effect of the position, number, shape of the holes. This model is extended to that of a stepped plate that takes into account the thickness step associated with the ring. Finally, a finite element simulation is presented in section 4. It summarizes the governing equations related to the coupling between the piezoelectric disc and plate. Frequency domain computations aims at compare the trends from the analytical model

and suggest possible ways to enhance the analytical models.

1. Structure geometry and governing equation

The structure under study is shown in Fig. 2 and consists in a circular steel plate coupled with a piezoelectric ring. The circular plate is characterized by its radius r_o, thickness d_p, Young's modulus E_p, density ρ_p, Poisson's ratio ν_p, corrected Young's modulus $E'_p = E_p/(1-\nu_p^2)$. The piezoelectric ring is characterized by its inner radius r_i, outer radius r_o, thickness d_r. The bonding layer between the piezo ring and the plate is usually less than 10 µm and such thickness compared to the plate thickness have a negligible effect on the global behavior. The geometric parameters and mechanical properties of the plate and ring are detailed in Table 1.

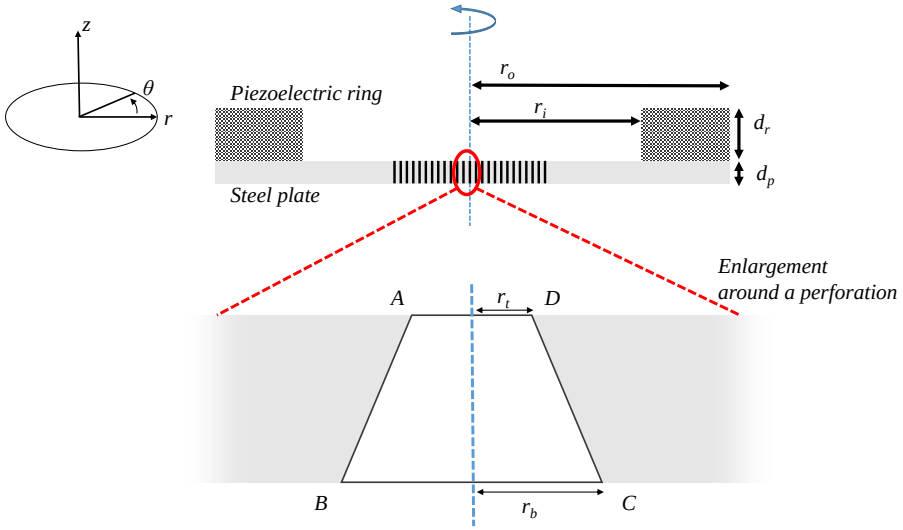

Figure 2: 2-D axisymmetric view of the atomizer : circular plate coupled with piezoelectric ring. Enlarged view of the perforated mesh and notations used to describe the motion of the hole

Figure 2 also shows an enlargement of the plate around a perforation. In the following, holes might have a conical shape where r_t is the top radius and r_b is the bottom radius. Four points denoted A, B, C, D will be used in the following to investigate the kinematics of the perforation.

Table 1: Mechanical and geometrical parameters of the circular plate and piezoelectric disc

	Plate	Piezoelectric ring
Mass density [kg.m^{-3}]	$\rho_p = 7850$	$\rho_r = 7500$
Young's Modulus [GPa]	$E_p = 205$	$E_r = 50$
Poisson ratio	$\nu = 0.3$	$\nu = 0.3$
Dimensions [mm]	$d_p = 0.1$, $r_i = 2.5$	$d_r = 0.3$, $r_o = 5$

Assuming thin plate ($d_p/2r_o \ll 1$), and small deformations, and considering that the origin of the frame matches with the center of the plate, the transverse displacement w of

the circular plate is $E'_p I_p \nabla^4 w - \Lambda'_p \omega^2 w = 0$ where ∇ is considered in polar coordinates (r, θ) with r the radial coordinate and θ the angular coordinate.

Thus, the complete solution to the fourth-order equation in polar coordinates is

$$w(r,\theta) = [EJ_n(\delta r) + FI_n(\delta r) + GK_n(\delta r) + HY_n(\delta r)]\cos(m\theta) \qquad (1)$$

where E, F, G, H are the integration constants to be determined from the boundary conditions, δ the wavenumber such as $\delta = \Lambda_p \omega^2 / EI$, n is the order of the Bessel and modified Bessel functions and m corresponds to the number of nodal diameters. In the following, $m = 0$ since the excitation is uniformly distributed along the contour and circumferential modes cannot be excited.

This modeling will be used for the assessment of the effective mass in section 2, and for the investigation of the volume change in a perforation in section 3.

2. Analytical modeling of the volume change above the perforated mesh

This section aims at correlate the variation of fluid above the perforated mesh to the modal behavior of the plate. The apparent mass of the plate is introduced analytically as a preliminary tool to evaluate working conditions of the device based on modal considerations.

2.1. Modeling of the effective mass

For a given distribution of transverse displacement on the plate, the amount of fluid above the plate is directly related to the effective mass of the vibrating plate, which is, in this case, given by the integral of the deflection over the surface of the plate. To avoid any discontinuity during the integration step, the perforations are temporarily neglected. The plate model introduced in Section 1 degenerates into the description of the dynamic behavior of circular plate clamped its contour and driven by a uniform out-of-plane unitary motion. Since the amplitude should remain finite at $r = 0$, the transverse displacement of the plate at any point on its surface is governed by $w = (EJ_0(\delta r) + FI_0(\delta r))cos(m\theta)$, where $m = 0$. The boundary conditions are $w(r = r_i) = 1$ and $d_r w(r = r_i) = 0$, and Fig. 3 shows the modal shapes that could possibly be excited according to these boundary conditions.

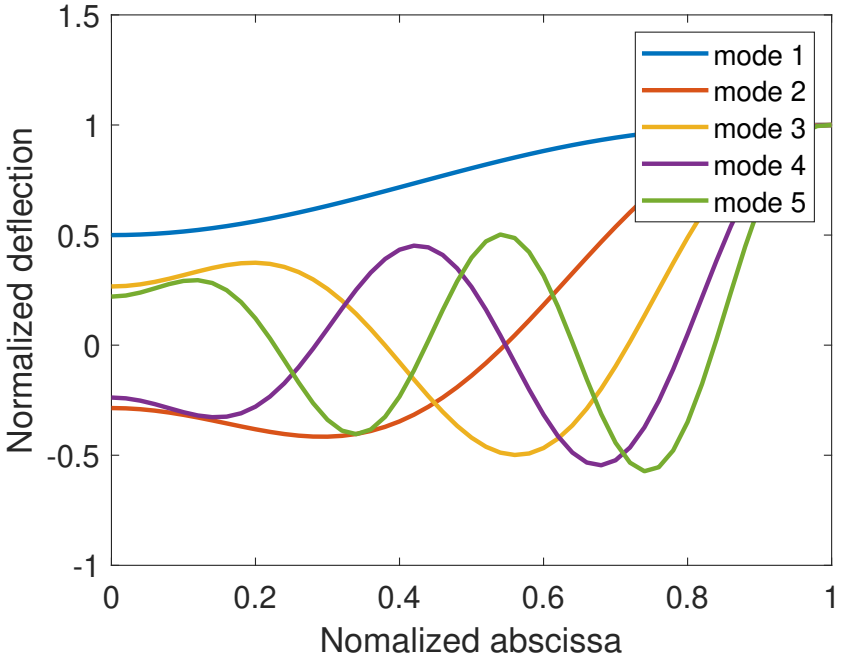

Figure 3: Modal shape of the circular plate clamped all around with dynamic displacement on its outer radius

The effective mass of the vibrating plate, which is, given by the integral of the deflection over the surface of the plate is expressed in cylindrical

coordinates is

$$\phi_\omega = \frac{1}{S}\int_0^l w\ r dr = \frac{4}{\delta r_i}\ \frac{I_1(\delta r_i)J_1(\delta r_i)}{I_1(\delta r_i)J_0(\delta r_i) + I_0(\delta r_i)J_1(\delta r_i)} \tag{2}$$

The roots of

$$J_0(\delta r_i)I_1(\delta r_i) + I_0(\delta r_i)J_1(\delta r_i) = 0 \tag{3}$$

are $\delta r_i \approx 3.19$; 6.30; 9.43; 12.57; 15.71, and enable to calculate the circular plate eigen frequencies as $\omega_i^p = \left(\frac{\delta r_i}{r_i}\right)^2 \sqrt{\frac{E_p' I_p}{\Lambda_p}}$

This quantity is frequency dependent and exhibits singularities associated with eigenmodes of the clamped plate. Further comments are made in the next subsection, dedicated to the study of this quantity according to some key design parameters that are flexural rigidity, thickness, and surfacic mass.

2.2. Parametric study

This subsection provides a parametric study over three relevant quantities associated with the plate, namely, its flexural rigidity $E_p' I_p$, thickness d_p, and surfacic mass Λ_p. The effective mass will be compared to that obtained from the set of parameters in Table 1, as a function of the normalized frequency $\tilde{f} = f/f_1$, where f_1 is the first eigenfrequency of the plate.

The effect of the variation of flexural rigidity is depicted in Fig. 4. The effective mass term is plotted for a plate whose flexural rigidity EI' varies from $\pm 20\%$ from the flexural rigidity $E_p' I_p$ of the initial setup. This change gives rise to a frequency shift of $\pm 10\%$ of the first eigenfrequency.

The effect of the variation of plate's thickness d_p is depicted in Fig. 5. The effective mass term is plotted for a plate whose thickness d_p' increases up to 5% thicker as the initial setup. This change gives rise to a frequency shift of $+10\%$ of the first eigenfrequency.

The effect of the variation of surfacic mass Λ_p' is depicted in Fig. 6. The effective mass term is plotted for a plate whose surfacic mass Λ_p' varies from $\pm 20\%$ from the surfacic mass Λ_p of the initial setup. This change gives rise respectively to a frequency shift of -11% to $+8\%$ of the first eigenfrequency.

2.3. Concluding remarks

This first modeling based on the effective mass of the plate illustrates the idea that the amount of fluid that is set into motion above the plate is directly related to its effective mass. This is introduced as a first parameter

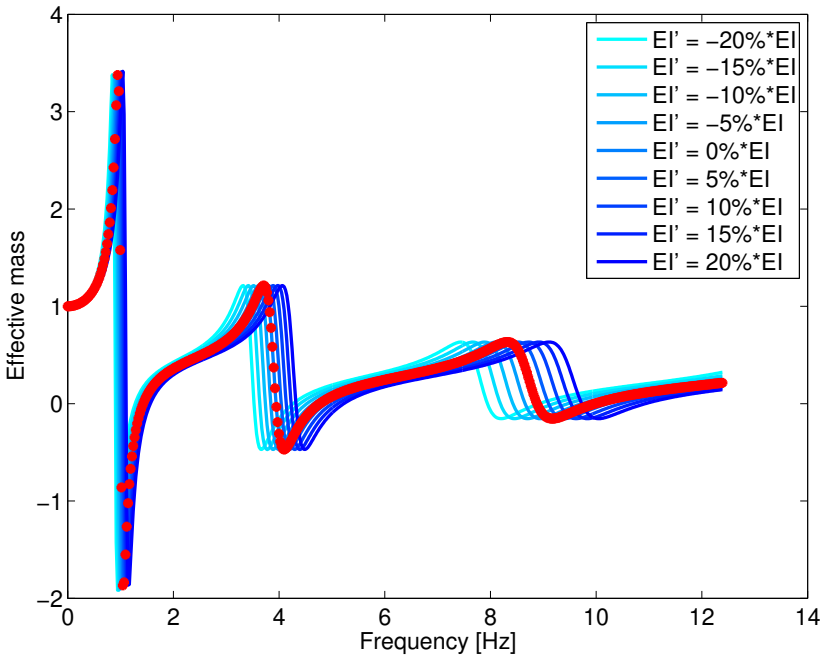

Figure 4: Effective mass of the clamped circular plate versus frequency with increasing flexural rigidity (from light to dark blue) and reference configuration (∗)

for the optimal design of the nebulizer.
The next section focuses on the study of shape and distribution of hole over the plate to maximize this pumping effect.

3. Modeling of the volume change in the perforated mesh

This section is dedicated to another key factor, which is the volume change occurring in apertures of the mesh. As the plate is driven by an harmonic motion, it bends and the over one period of excitation, the volume change in one hole is cyclic. Indeed, when the volume of the aperture increases, the pressure decreases, that makes the liquid flowing from upstream the mesh to inside the aperture. While the volume of the aperture decreases, the pressure in it increases and pushes the amount of fluid downstream the mesh. This volume change in the apertures contributes to the pumping effect and results in the ejection of the droplet.

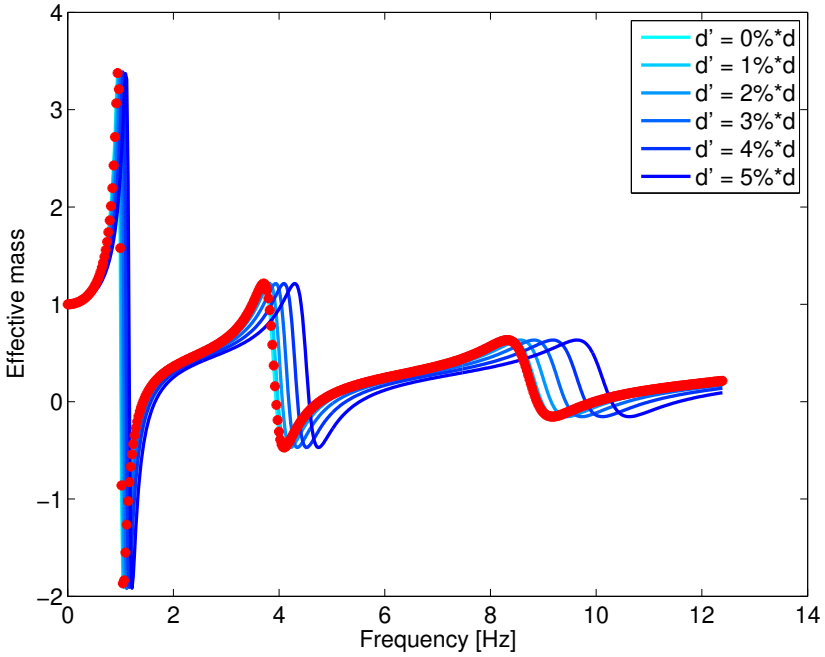

Figure 5: Effective mass of the clamped circular plate versus frequency with increasing d (from light to dark blue) and reference configuration ($*$)

3.1. Analytical modeling of the volume change in one single perforation

This section provides an insight on the modeling of the volume change in the apertures based on a plate model. It introduces the calculations for one single apertures, then generalizes it to multiple apertures. This model is built in such a way that it enables to assess i) the influence of the shape of the aperture (whose initial cross section is either rectangular or trapezoidal) and ii) the influence of the position of the hole on the change of volume in it.

The flatness of the plate, defined as the ratio $d_p/2r_i \ll 1$ suggests that the thin plate assumption is valid, and that its transverse motion will be adequately described by the Kirchhoff formulation.

The motion of a wall of a perforation is illustrated in Fig. 7

Figure 2 shows the cross section of the plate with one single aperture whose centroid abscissa is located at x_M. In the following, the volume change of the aperture is calculated from the volume change of the truncated cone change of area of the trapezoid formed by points A, B, C, D. Assuming

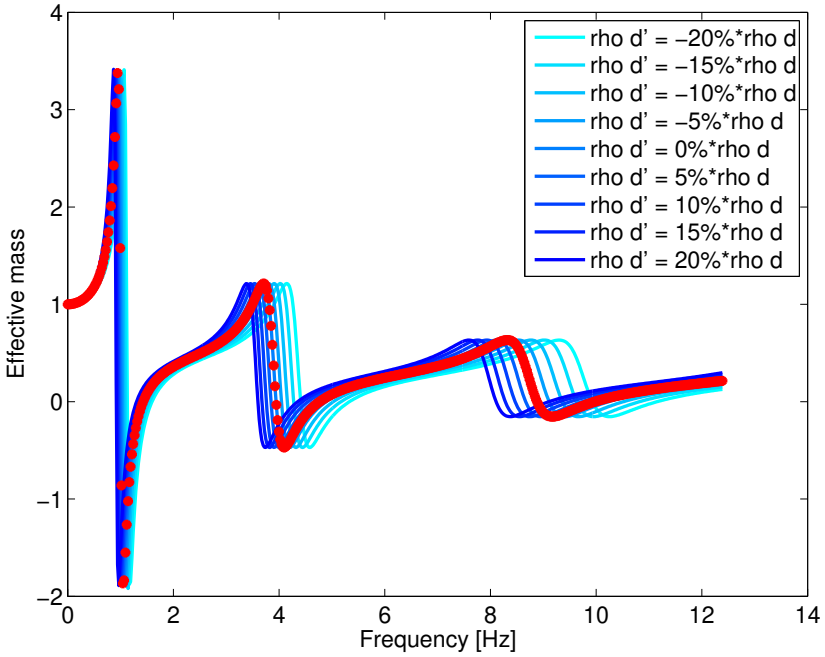

Figure 6: Effective mass of the clamped circular plate versus frequency with increasing surfacic mass (from light to dark blue) and reference configuration ($*$)

Kirchhoff hypothesis, plane sections perpendicular to the neutral axis before deformation remain plane and perpendicular to the neutral axis after deformation, deformations are small, and the plate is made of linear elastic material.

The plate is considered to be aligned along the $r-$ axis, and its center matches with origin of the coordinates. Its deflection is described by a function $w(r)$ which governs the transverse displacement of the neutral fiber, as (1). For any point p of coordinates $X = (r_p, z_p)$ before deformation, its coordinates after deformation are $X' = (r_p - z_p \sin\phi, w + z_p \cos\phi)$, where ϕ denotes the rotation of the cross-section, expressed as $\phi = dw/dr$. It is outlined that each point moves according to a transverse and a longitudinal component, and according to the small deformation assumption, the displacement function may be simplified as $X'' = X' - X = (-z_p\phi, w)$.

This approach enables to calculate the displacement and rotation of each point considered to deduce the in-plane and transverse component of their respective motion. This will be done in the case of a cylindrical and conical

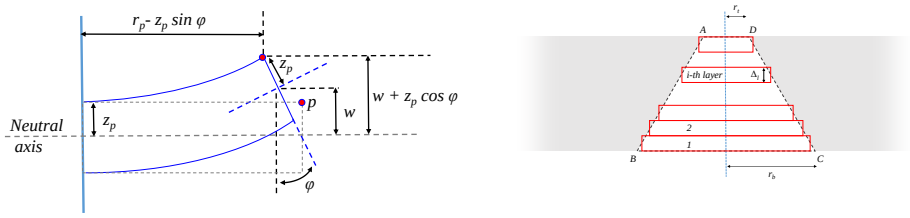

(a) (b)

Figure 7: Notations associated with bending kinematics of the plate cross-section, before (dotted line) and after deformation (solid line) (a), and discretization of the variable cross-section perforation (b).

perforation, whose centroid abscissa is located either $x_M = 0.2r_i$ and $x_M = 0.4r_i$. These four cases illustrate the effect of shape of the perforation, and the influence of its position. These are presented an compared with finite element computation in the next next section.

3.2. Finite element validation

A 2D- axisymmetric model of the circular plate is implemented using the solid mechanics module. The material is considered as isotropic and prescribed harmonic displacement is specified on the outer edge to mimic the deflection imposed by the piezo. Although this is a simplified modeling, it is enough to understand the kinematics of the perforation rather than describing the nature of the coupling between the piezo ring and the plate. The complete mesh resulted in 100 domain elements and 110 boundary elements. Running the frequency study from 0 to 1 Mhz with a frequency step of 2 kHz resulted in a computation time of approximately 30s for 1010 degrees of freedom.

From the mechanical properties and geometric parameters of the circular plate presented in Table 1, the analytical in-plane and transverse components of point A are successfully compared to a finite element computation, as shown is Fig. 8. The frequencies at which there the direction of motion changes correspond to the eigenfrequencies of the plate. This effect is perfectly recovered for two positions.

Additional variables describing the dynamic behavior are also introduced to describe the surface change of the trapezoid formed by ABCD. Denoting

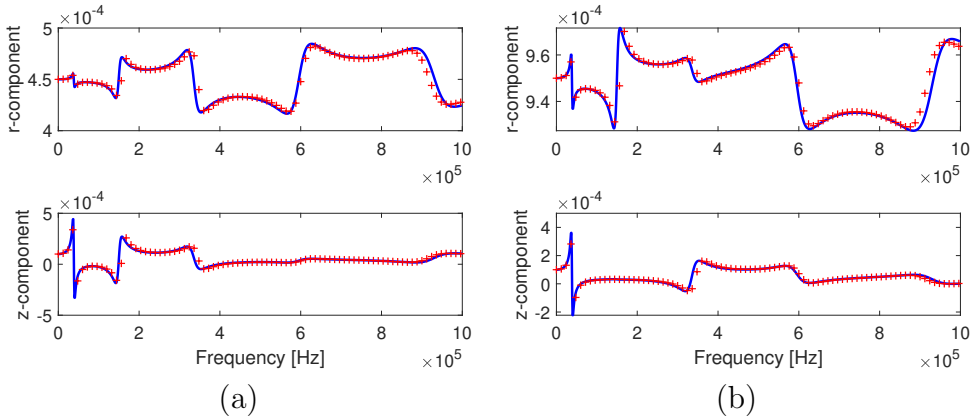

Figure 8: In-plane and out-of-plane components of the motion of point A, analytical (−) and finite element comparison (+), cylindrical perforation located at (a) $x_M = 0.2r_i$, and (b) $x_M = 0.4r_i$

r_t* the dynamic top radius of the hole, and r_b* the dynamic bottom radius of the hole, these quantities are compared to a finite element computation and normalized by the static radii r_t and r_b respectively, as shown in Fig. 9. Again, significant changes of variation of these parameters occur at each eigenfrequency, and well recovered in frequency and amplitude.

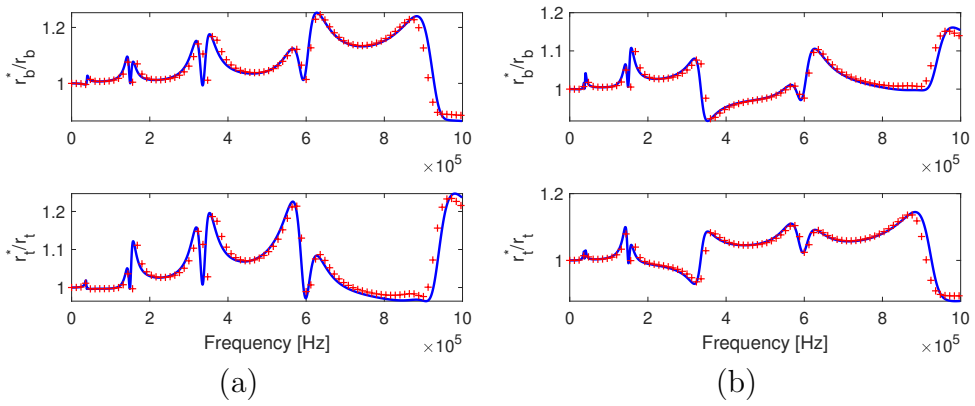

Figure 9: Relative length variation of dynamic bottom radius r_b^*/r_b and top radius r_t^*/r_t, analytical (−), finite element comparison (+), cylindrical perforation located at (a) $x_M = 0.2r_i$, and (b) $x_M = 0.4r_i$

We can note that in the case of a perforation in the middle of the plate ($x_M = 0$), if the plate is subjected to an harmonic excitation, the upper and

lower faces of the hole increase and decrease in an opposite way to each other, so that r_t^* increases while r_b^* decreases and inversely during the second phase of the cycle.

Finally, the surface change ΔS of the trapezoid is frequency dependent and exhibit significant variations around the eigenmodes of the plate. For the sake of clarity, we introduce the normalized dynamic surface change $\Delta S = S^*/S_0$, where S^* is the frequency dependent surface change and S_0 is the initial cross-section area of the perforation. This quantity is compared to the direct integration from the finite element model and illustrated in Fig. 10 for a cylindrical perforation, and in Fig. 11 for a conical perforation.

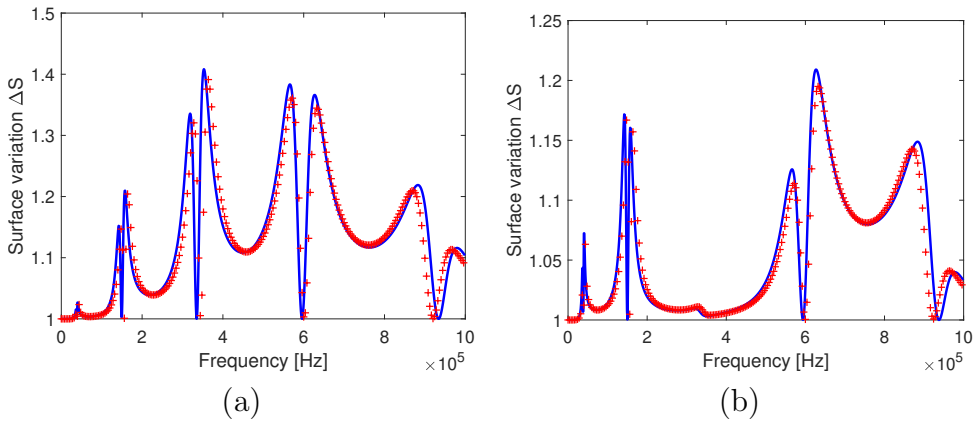

Figure 10: Relative surface variation ΔS, analytical (−), finite element comparison (+), cylindrical perforation located at (a) $x_M = 0.2r_i$, and (b) $x_M = 0.4r_i$

Although the calculation for the cylindrical perforation is straightforward and exact, the one for a conical is approximated. In this approach, the total height of the perforation is divided into n slices each of constant height $\Delta h = d_p/n$, and of variable width depending on the altitude of the layer$z = \Delta h(i-1)$ where i is the layer label ($i = 1, 2, \ldots, n$), as shown in Fig. 7. The total surface change is thus obtained by summation as $S^* = \sum_n S_n(z)$. In the following, n is chosen as 10.

Very good consistency is reached for both cylindrical and conical perforation versus finite element. From the previous developments, the area is calculated assuming an isocele trapezoid, meaning that the two legs have the same length, and that it is symmetric with respect to the axis passing through points M_t and M_b. In this way the volume of the cone is easily calculated by revolving this surface around the symmetry axis. In case of a cylindrical

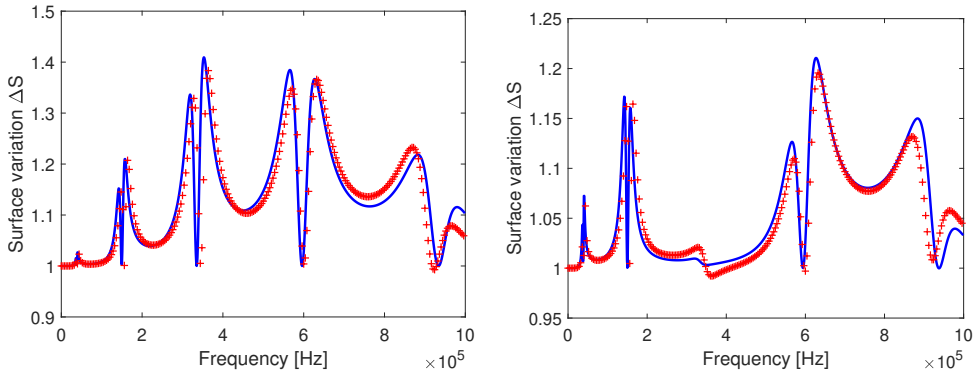

Figure 11: Relative surface variation ΔS, analytical ($-$), finite element comparison ($+$), conical perforation located at (a) $x_M = 0.2r_i$, and (b) $x_M = 0.4r_i$

perforation, the upward and downward bending of the plate causes the initial rectangle to deform as a trapezoid with straight edges. However, when considering a conical perforation, the bending causes the initial trapezoid to deform in a asymmetric shape whose area cannot be calculated under the isocele trapezoid assumption. This loss of precision is compensated by the step of integration over several layers.

In addition to these comments, the complex deformation experienced by the trapezoid when the plate bends is illustrated in Fig. 12

The volume change in one single perforation is finally deduced from the quantities presented above, and illustrated for a cylindrical perforation, and a conical perforation. The normalized dynamic volume change $\Delta V = V^*/V_0$, where V^* is the frequency dependent volume change, and V_0 is the initial volume of the perforation. This dynamic volume change is illustrated in Fig. 13 in the case of one single cylindrical perforation compared to a conical one, either located at $x_M = 0.2r_i$, and $x_M = 0.4r_i$. For the two positions, it is clearly seen that the conical and cylindrical shape offer very similar variation of volume. This is demonstrated in terms of amplitude of the volume change, as well as on the frequency range. Actually, the the volume change of the perforation is located mainly around the eigenfrequencies of the plate.

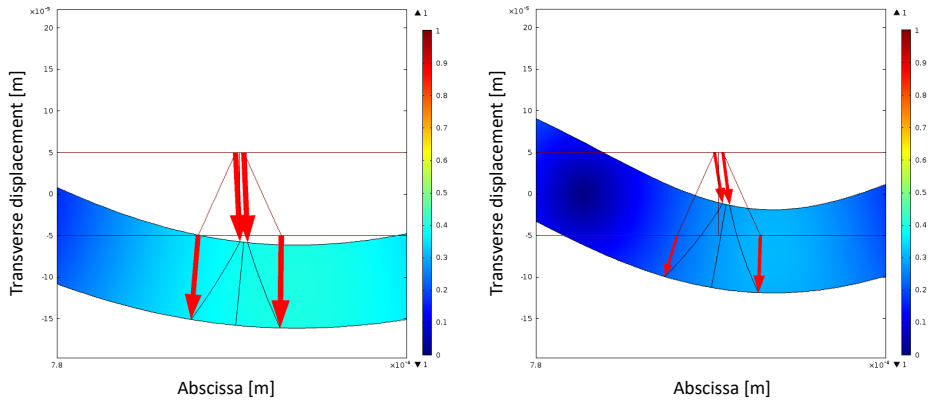

Figure 12: Displacement field associated to the edges of the conical perforation located at $x_M = 0.4r_i$ at 0.32 MHz (left) and 0.97 MHz (right)

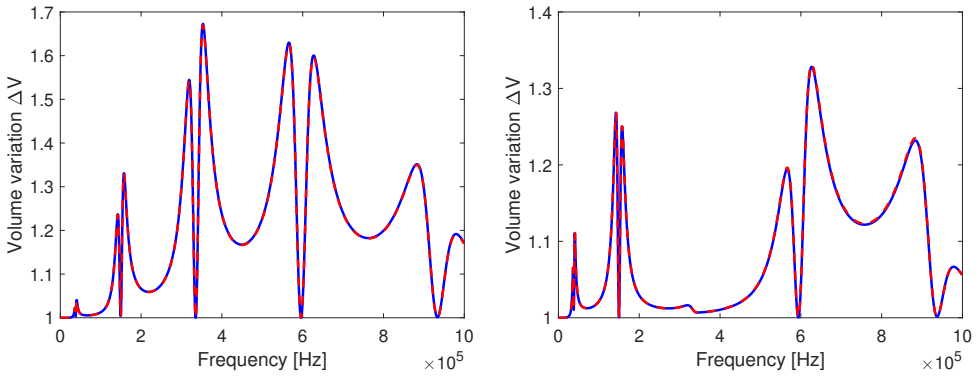

Figure 13: Relative volume variation ΔV in a single perforation located at $x_M = 0.2r_i$ (a) $x_M = 0.4r_i$ (b), conical ($-$) and cylindrical perforation ($--$)

3.3. Effect of the position of a single hole on volume variation

For this investigation, the x-coordinate of the center line x_M of the perforation is moved from $x_M = 0$ to $x_M = 0.6r_i$. The normalized volume variation calculated from the analytical model is shown for a cylindrical hole in Fig. 14 and for a conical hole in Fig. 15.

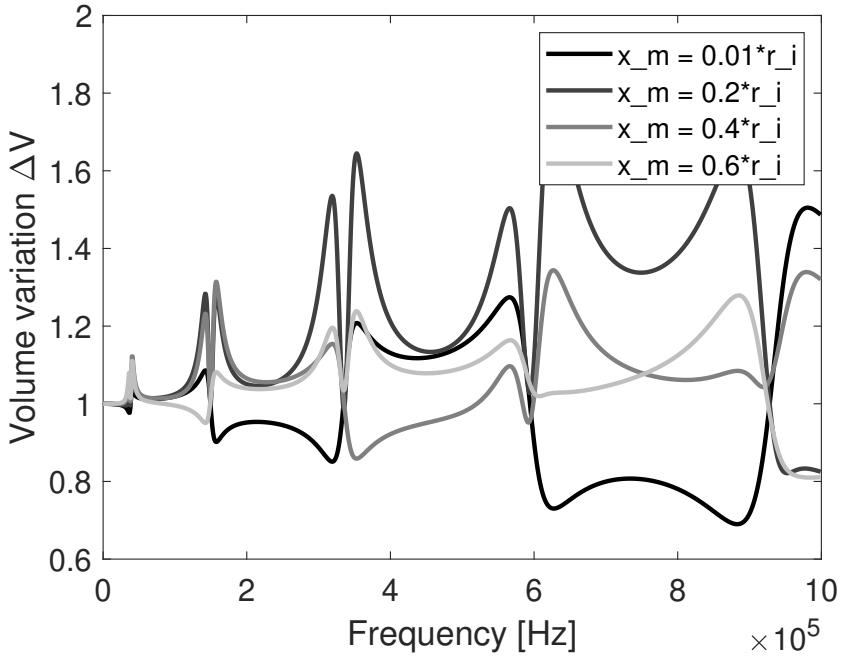

Figure 14: Analytical normalized volume variation ΔV of one single cylindrical perforation versus frequency, for different positions

It is observed in Fig. 14 that the volume variation associated with the different modes exhibit changes of behavior resulting from the combination of in-plane an out-of plane displacements of the initial trapezoid. Looking at Fig. 3 helps in commenting these trends. Regarding the first mode, for which the transverse amplitude of vibration decreases while moving away from the middle, the volume variation also decreases. The same comment can be formulated for the second mode, which suggest that the maximum of volume change diminishes far away from the middle. However, the volume change around the third mode shows that similar volume changes appear for $x_M = 0.06r_i$ and $x_M = 0.036r_i$. This could be partially assumed from the analysis of Fig. 3, and it is confirmed with this model, that takes into account the dynamic deformation of the hole.

Despite the more complex kinematic of the perforation, the same comments apply in the case of a conical hole, for which the volume variation is illustrated in Fig. 15.

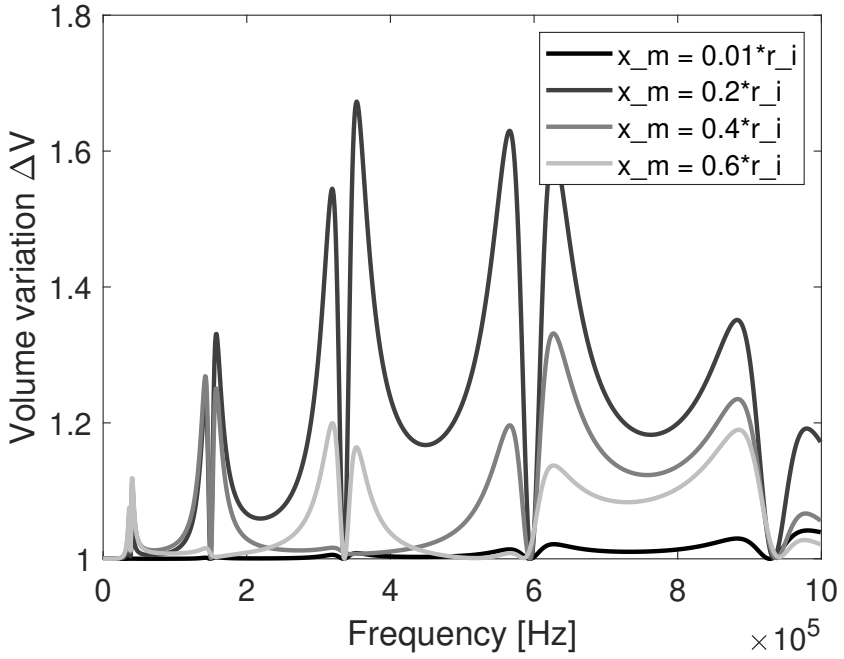

Figure 15: Normalized volume variation ΔV of the conical perforation versus frequency

3.4. Effect of the distribution of holes on average volume variation

Introducing the average volume variation ΔV_m brings a new indication about the volume variation provided by several perforations. Two distributions are considered ; 9 perforations between 0 and $r_i/2$, and 17 perforations between 0 and r_i. The spacing is regular and the distance between the mid axis of two neighbouring perforations is chosen as $3r_b$ to avoid overlapping. The comparison of the average volume variation provided by these two distributions is shown in Fig. 16, for conical and cylindrical perforations. Again, the shape of the perforation doesn't affect the volume variation. Also, the comparison suggests that the most favorable configuration is to have perforations in the center of the plate rather than over the entire surface. This is predictable since the low frequency modes having their maximum of deflection in the center of the plate are most likely to contribute to the kinematics rather than the high frequency mode having multiple nodal lines.

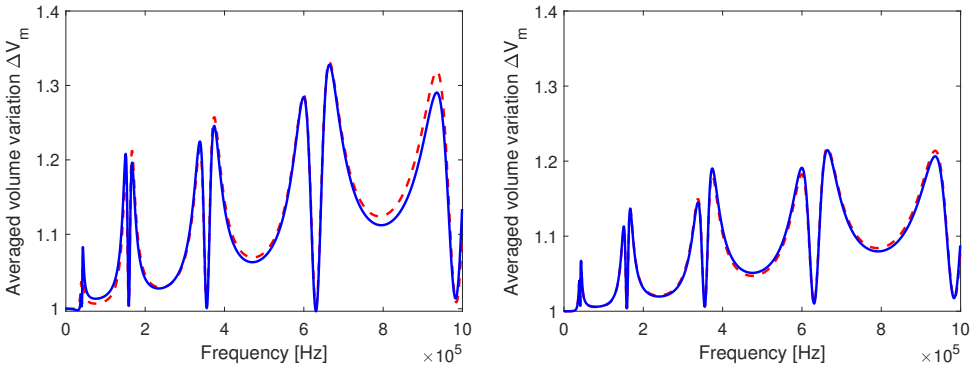

Figure 16: Average volume variation ΔV_m in perforations distributed as $0 \leq x_M \leq 0.5 r_i$ (a), and $0 \leq x_M \leq r_i$ (b), conical ($-$) and cylindrical perforation ($--$)

3.5. Volume variation experienced by perforation on stepped circular plate

In this section, the investigation introduced in section 3 is extended to a stepped plate. This is done within the assumption of thin plate and small deformation. The circular plate with piezoelectric ring attached on it is modeled as a stepped plate whose cross section is represented in Fig. 2. Two regions are considered: first is associated with the internal plate $0 < r < r_i$ whose surfacic mass is Λ_1 and flexural rigidity is EI_1, second is associated with the ring $r_i < r < r_o$, whose surfacic mass is Λ_2 and flexural rigidity is EI_2. According to the solution form given in section 1, the transverse displacement w_1 in region 1 should remain finite in $r = 0$ so it is written

$$w_1(r) = E_1 J_n(\delta_1 r) + F_1 I_n(\delta_1 r) \tag{4}$$

whereas for region 2 associated with the ring, the full form must be considered, so the transverse displacement w_2 is written

$$w_2(r) = E_2 J_n(\delta_2 r) + F_2 I_n(\delta_2 r) + G_2 K_n(\delta_2 r) + H_2 Y_n(\delta_2 r) \tag{5}$$

where $E_1, F_1, E_2, F_2, G_2, H_2$ are the integration constants to be determined from the boundary conditions, δ_1 the wavenumber in region 1 such as $\delta_1 = \Lambda_1 \omega^2 / EI_1$, δ_2 the wavenumber in region 2 such as $\delta_2 = \Lambda_2 \omega^2 / EI_2$. Four boundary conditions are stated at $r = r_i$ and given by the continuity of displacement $w_1(r_i) = w_2(r_i)$, rotation $d_r w_1(r_i) = d_r w_1(r_i)$, bending moment in radial direction $M_1(r_i) = M_2(r_i)$, and transverse shearing force

$Q_1(r_i) = Q_2(r_i)$, respectively calculated as $M = -EI(d_r^2 w + \nu/r\ d_r w)$ and $Q = EI d_r(d_r^2 w + 1/r\ d_r w)$. Two additional boundary condition on the outer radius must also be specified.

In the following, region 1 has $\Lambda_1 = \Lambda_p$ and $EI_1 = EI_p$, and region 2 has equivalent properties associated with both plate and ring, that are introduced in the surfacic mass as

$$\Lambda_2 = d_p(\rho_p d_p + \rho_r d_r)/(d_p + d_r)$$

as well as in the flexural rigidity as

$$EI_2 = EI_p(1 + t\gamma^3 + 3(1+\gamma)^2 t\gamma/1 + t\gamma)$$

with $t = E_r/E_p$ and $\gamma = d_r/d_p$. Note that for a given thickness, the flexural rigidity of the plate is much higher than that of the ring, so the ring is introduced as an additional layer on the plate.

The consistency of this approach is verified by considering a clamped boundary condition with static deflection on the outer radius ($w_2(r_o) = 1, d_r w_2(r_o) = 0$), and by plotting the frequency response between two points located at $0.3r_i$ and $0.9r_o$, for two different geometries : $d_r = 0.1$ mm and $d_r = 0.3$ mm. The analytical result is compared with the finite element computation in Fig. 17. Although the first case shows excellent agreement over the whole frequency range, the second case exhibits a validity limit around 0.5 MHz after which the resonance frequencies are overestimated. These high frequency discrepancies are understood since *i*) the thin plate assumption is considered valid as long as the flatness of the plate satisfies $\varepsilon = (r_o - r_i)/d_r \ll 0.1$, that is $\varepsilon = 0.04$ for $d_r = 0.1$ mm, and $\varepsilon = 0.12$ if $d_r = 0.3$ mm, and *ii*) the continuity conditions at $r = r_i$ stated above become questionable when $\gamma = 3$, which corresponds to a step with a thickness ratio 1:4.

The two-dimensional frequency responses are given in Fig. 18, as the amplitude of transverse displacement at different locations along r, and versus frequency. It is seen that increasing the thickness of the ring stiffens the whole structure, resulting in a different distribution of eigenfrequencies. This representation gives a visualization of local maxima of displacement to conveniently identify frequency ranges versus displacement distribution.

From this modeling enriched by the contribution of the ring, the averaged volume variation ΔV_m is calculated for the two same distributions of holes as

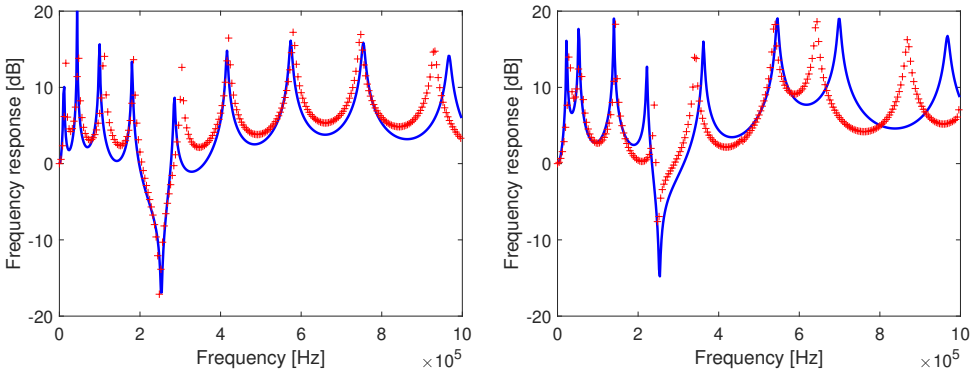

Figure 17: Frequency response of the clamped circular stepped plate $d_r = 0.1$ mm (a), and $d_r = 0.3$ mm (b), analytical (−), finite element comparison (+)

previously (9 perforations between 0 and $r_i/2$, and 17 perforations between 0 and r_i). It is shown in Fig. 19. The conical case is not represented. Again, the comparison suggests that the most favorable configuration is to have perforations in the center rather than over the entire surface of the internal plate. It is also seen that increasing the thickness of the ring brings a significant increase of the volume variation around 0.4 MHz.

3.6. Concluding remarks

This section provides a parametric study of some key geometrical parameters of the mesh itself, namely their shape, and their location along the radius.

A simple analytical model describing the volume variation is presented and shows excellent agreement with finite element simulation. Investigating the dynamic volume variation versus frequency for different position and different number of perforations shows that the shape of the perforation, either cylindrical of conical doesn't bring an increased volume variation. However the geometry nozzle becomes critically important when considering the nature of the flow downstream the mesh, and has a significant influence on the flow regime, discharge coefficient, surface tension, frictional effects and finally influences most the droplet formation, breakup, and ejection. Regarding the potions of holes over the plate, it is shown that the distribution providing the highest averaged volume variation is that of holes in the center of the plate rather than on the whole surface.

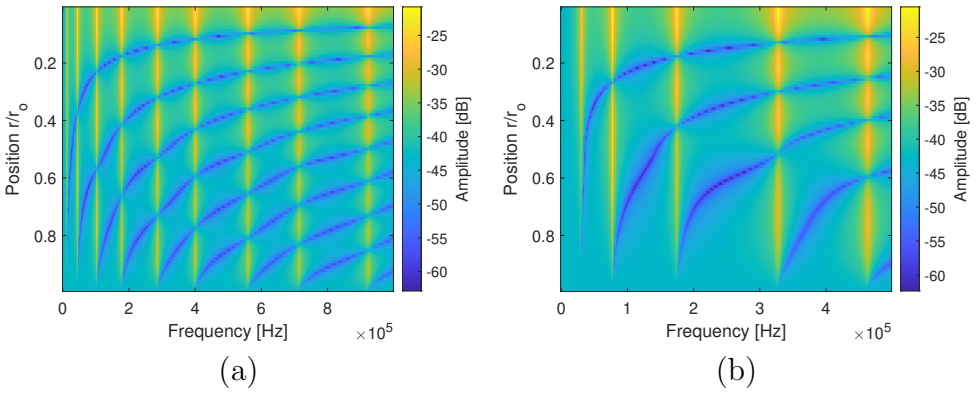

Figure 18: Two-dimensional frequency response of the clamped circular stepped plate $d_r = 0.1$ mm (a), and $d_r = 0.3$ mm (b) in their respective frequency range of validity

From this preliminary modeling, it appears that this description of the volume variation is robust and versatile enough to assess accurately the dynamic volume variation occurring in the mesh.

4. FEM modeling including piezoelectric component

This sections presents a finite element model of the nebulizer. The latter aims at confirming the trends identified above and suggest possible ways to enhance the analytical model.

4.1. Finite Element model

A two-dimensional axisymmetric model of the mesh nebulizer was build. It consists in one solid domain and one piezoelectric domain, as illustrated in Fig. 20. The cylindrical coordinate system is such that the origin coincides with the bottom left corner of the domain. The mechanical properties of both domains are summarized in Table 1 and Table 2.

Regarding the coupling and actuation mechanism, the piezoelectric component converts the electrical signal into mechanical energy. This transduction relating the electric field, electrical displacement, stresses and strains can be written in the stress-charge representation as:

$$\sigma = c_E.\varepsilon - e^T.\mathbf{E} \tag{6}$$

$$\mathbf{D} = e.\varepsilon + \varepsilon_S.\mathbf{E} \tag{7}$$

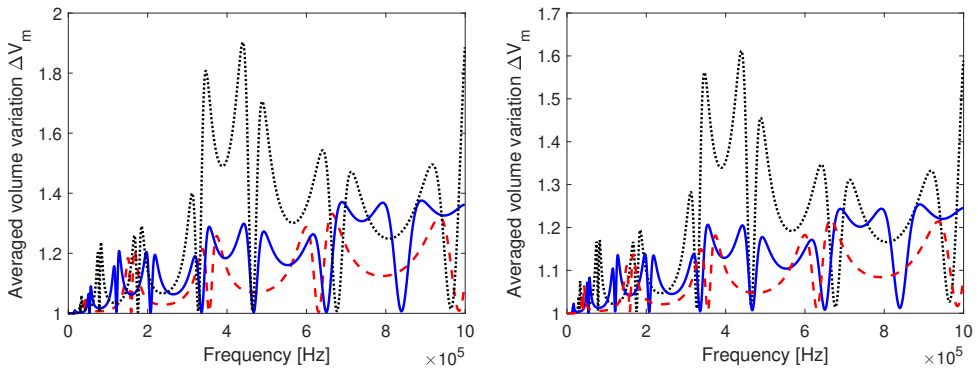

Figure 19: Average volume variation ΔV_m in cylindrical perforations distributed as $0 \leq x_M \leq 0.5r_i$ (a), and $0 \leq x_M \leq r_i$ (b), internal plate only ($--$), stepped plate with thickness ration $\gamma = 2$ ($-$) and $\gamma = 3$ ($\cdots$)

where σ is the mechanical stress ([N/m^2]), ε is the strain ([1]), c_E is the elasticity matrix ([Pa]) in the form of a rank 4 tensor, e is the coupling matrix ([C/m^2]) in the form of a rank 3 tensor, E is the electric field defined as the electric force per unit charge, D is the electrical displacement ([C/m^2]), and ε_S is the dielectric matrix ([F/m]) in the form of a rank 2 tensor.

When the piezoelectric component is subjected to a periodic electric potential ($E = -\nabla V$ where $V[V]$ is the electric potential), it vibrates and transmits the energy to the steel plate. In this way writing the plate equation coupled to that piezoelectric component yields :

$$\mathrm{div}(\sigma) + F_p e^{i\omega t} = -\rho\omega^2 w \tag{8}$$

$$\mathrm{div}(\sigma) = \rho\frac{\partial^2 w}{\partial t^2} + F_p \tag{9}$$

$$\mathrm{div}(D) = \rho_v \tag{10}$$

where ρ is the mass density of the piezoelectric material ([kg/m^3]), $\omega = 2\pi f$ with f the excitation frequency ([Hz]), u is the displacement response (u, v, w) ([m]), F_p is the volume force ([N]), ρ_v is the volume charge density ([C/m^2]).

As the analysis involves piezoelectric material and linear elastic material, two sets of boundary conditions are specified. Mechanical boundary conditions consist of a free edge on the plate circumference, while the other

Table 2: Electro-mechanical parameters of the piezoelectric component (PZT-4)

Elasticity	Coupling matrix	Relative permittivity
$C_{11}^E = 1.53e11$; $C_{12}^E = 9.84e10$,	$e_{31} = -4.73$	$\varepsilon_{11} = 796.5$
$C_{13}^E = 9.31e10$; $C_{33}^E = 1.28e11$,	$e_{33} = 15.25$	$\varepsilon_{33} = 762.9$
$C_{44}^E = 2.38e10$; $C_{12}^E = 2.77e10$	$e_{15} = 13.09$	

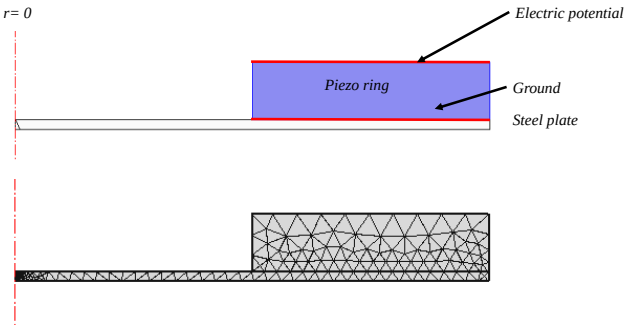

Figure 20: 2D axisymmetric finite element model of the perforated coupled with piezoelectric ring, and associated mesh

surfaces are free. For the electrical boundary conditions, the piezoelectric ring was actuated by applying an electric potential $V_0 = 80V$ of harmonic signal on its upper face, while its bottom face was specified as ground.

In this study, the piezo is polarized along the $+z$ direction. Both the plate and piezo are meshed using triangular elements and resulted in 307 triangular elements and 1721 degrees of freedom.

4.2. Frequency domain computations

In order to confirm the trend identified from the analytical model, that suggests to distribute the holes in the middle of the plate rather than over the whole surface, a finite element computation is performed to check the average displacement amplitude over the two regions : either $[0; 0.5r_i]$ and $[0; r_i]$. The

result is shown in Fig. 21 and shows that the center region experiences larger displacement than the whole surface.

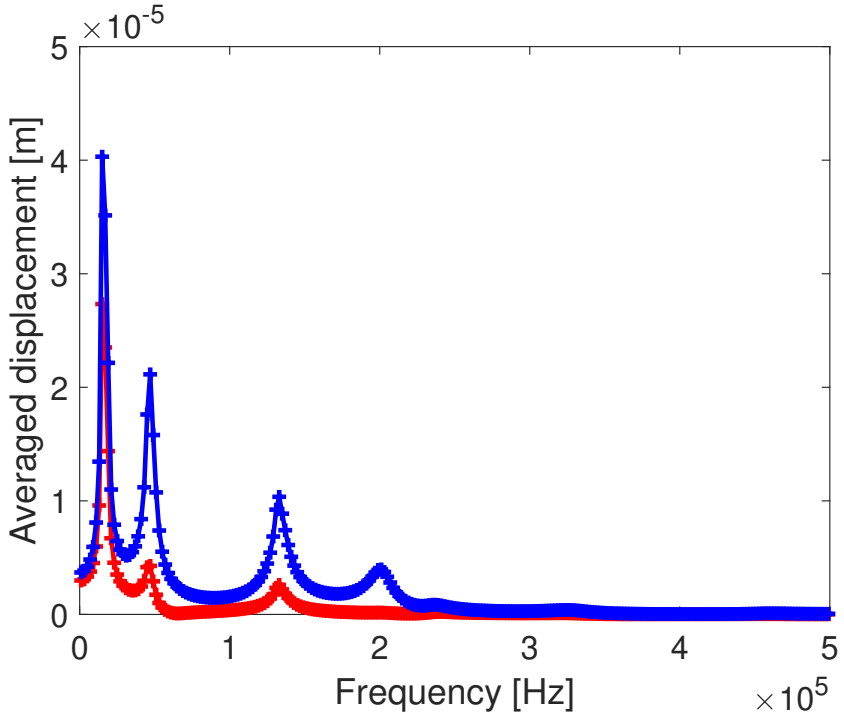

Figure 21: Finite element computation of the averaged transverse displacement over the top surface of the internal plate for two regions : $[0; 0.5r_i]$ $(-+-)$ and $[0; r_i]$ $(-+-)$

The frequencies associated with maxima of displacement are clearly identified and illustrated in Fig. 22. These are respectively associated with with the first mode of the coupled structure, first mode of the internal plate, and higher mode for which the ring starts contributing to the dynamic of the overall structure. Although the analytical is illustrated using clamped boundary conditions, these kinematics are available through the analytical model.

The assessment of the volume variation occurring multiple perforations would require the full three-dimensional modeling of the structure. The result of such a lengthy computation is not of interest in this paper. The specific role of the piezoelectric ring is to induce vibrations of the perforated mesh in the form of bending moment distributed along the bottom face of the ring. This complex boundary condition could be introduced analytically.

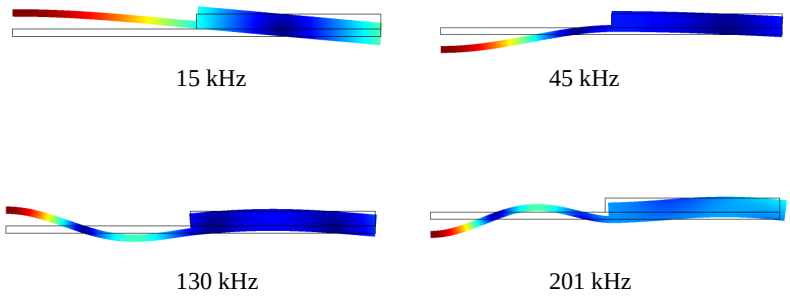

Figure 22: Modal shapes associated with maximum values of volume change in Fig. 21

Conclusion

This work suggests a comprehensive study of the mechanical behavior of an ultrasonic mesh atomizer consisting of a circular perforated plate surrounded by a piezoelectric ring. The actuation of the piezoelectric ring induces vibrations in the perforated plate and the variation in volume within each perforation creates a pumping effect which allows fluid to be pulled into the holes and then released on the other side as droplets. Therefore this pumping appears to be a key aspect in the design and working conditions of such devices. The proposed models are based on linear formulations, small deformation and thin plate assumptions. Finite element comparisons are systematically given to show the gives excellent trends for a relatively moderate level of complication.

The first model is that of a plate whose effective mass density in related to the amount of fluid set into motion downstream the plate. Based on modal considerations, it is shown that the first an second mode are associated with the greatest efficiency. Although the volume change above the perforated mesh is one factor affecting the performance of atomization, the change of volume in apertures of the mesh is also investigated.

In this way, a second model is built and focuses on the kinematics of the perforations, according to their shape and location along the radius. Without going into the details of a micromechanical description, it is shown that the volume variation is closely related to the mode shapes of the plate. Par-

ticularly, the volume variation in a single perforation is increased when it is located on a maximum of curvature. It is shown that the shape of the perforation, either cylindrical of conical doesn't bring a significant increase in volume variation. However, one should outline that the geometry nozzle has significant influence on the flow regime, discharge coefficient, surface tension, frictional effects and finally influences most the droplet formation, breakup, and ejection, that is not investigated in this paper. It is also shown that distributing the holes in the middle of the plate provides a higher average volume variation than distributing them over the whole surface. Successive finite element comparisons confirm that this description of the volume variation is robust and versatile enough to assess accurately the dynamic volume variation occurring in the mesh.

A third model enriches the second model with a stepped plate to mimic the piezo ring as an additional mass and flexural rigidity on the contour of the plate. This model accurately captures the first modes of vibrations for a ring up to four times thicker than the plate, that is a realistic geometry. More sophisticated kinematics are then reached and complete the observations of the second model. The frequency limits of the models are identified to offer finite element validations at each stage of construction. It is emphasized that this model gives excellent trends for a relatively moderate complexity.

A fourth model is finally proposed and relies on finite element frequency domain computation. It illustrates the response of the plate when excited by the piezo actuated by electric potential. The kinematics observed are indeed those described in the stepped plate model and confirms the relevance of the modeling in terms of trends. Formal comparison with analytical model would require a better introduction of the coupling between the ring and plate in the form of a distributed moment along the radius. This study could be supplemented by investigating the contribution of the the piezoelectric ring to the overall dynamic of the device, or by optimizing the electromechanical properties of the piezo ring to maximise the deflection of the internal plate.

CRediT author statement

Pascal Fossat: Conceptualization, Methodology, Software, Writing - original draft, Writing - review & editing. **Mohamed Ichchou**: Writing - review & editing, Validation, Supervision, Project administration, Funding acquisition. **Olivier Bareille**: Supervision, Project administration, Funding acquisition.

Acknowledgment

This work was supported by the LabEx CeLyA (Centre Lyonnais d'Acoustique, ANR-10-LABX-0060) of Université de Lyon, within the program "Investissements d'Avenir" (ANR-11-IDEX-0007) operated by the French National Research Agency (ANR).

References

[1] A. J. Yule, Y. Al-Suleimani, On droplet formation from capillary waves on a vibrating surface, Proceedings: Mathematical, Physical and Engineering Sciences 456 (2000) 1069–1085.

[2] R. Dhand, Nebulizers that use a vibrating mesh or plate with multiple apertures to generate aerosol, Respiratory care 47 (2003) 1406–16; discussion 1416.

[3] T. Ghazanfari, A. Elhissi, Z. Ding, K. Taylor, The influence of fluid physicochemical properties on vibrating-mesh nebulization, International journal of pharmaceutics 339 (2007) 103–11.

[4] R. Dhand, Comparison of vibrating mesh / plate devices and conventional jet and ultrasonic nebulizers in vitro comparisons of efficiency in aerosolizing solutions in vitro comparisons of efficiency in aerosolizing suspensions scintigraphic evaluation of pulmonary deposition of aerosol clinical evaluation of d.

[5] W. H. Finlay, Chapter 8 - aqueous aerosol delivery devices, in: W. H. Finlay (Ed.), The Mechanics of Inhaled Pharmaceutical Aerosols (Second Edition), Academic Press, London, second edition edition, 2019, pp. 183–212.

[6] V. K. Patel, F. Kyle Reed, R. Kisner, C. Peng, S. Moghaddam, A. Mehdizadeh Momen, Novel Experimental Study of Fabric Drying Using Direct-Contact Ultrasonic Vibration, Journal of Thermal Science and Engineering Applications 11 (2018). 021008.

[7] K. Söllner, Experiments to demonstrate cavitation caused by ultrasonic waves, Trans. Faraday Soc. 32 (1936) 1537–1539.

[8] R. Rajan, A. Pandit, Correlations to predict droplet size in ultrasonic atomisation, Ultrasonics 39 (2001) 235–255.

[9] M. Eslamian, N. Ashgriz, The effect of atomization method on the morphology of spray dried particles, Journal of Engineering Materials and Technology 129 (2007) 130–142.

[10] N. Maehara, S. Ueha, E. Mori, Influence of the vibrating system of a multipinhole-plate ultrasonic nebulizer on its performance, Review of Scientific Instruments 57 (1986) 2870–2876.

[11] C. Fox, X. Chen, S. McWilliam, Analysis of the deflection of a circular plate with an annular piezoelectric actuator, Sensors and Actuators A: Physical 133 (2007) 180–194.

[12] D.-A. Wang, C.-H. Cheng, Y.-H. Hsieh, Z.-X. Zhang, Analysis of an annular pzt actuator for a droplet ejector, Sensors and Actuators A: Physical 137 (2007) 330–337.

[13] S. I. E. Lin, The theoretical and experimental studies of a circular multi-layered annular piezoelectric actuator, Sensors and Actuators A: Physical 165 (2011) 280–287.

[14] Y. Cai, J. Zhang, C. Zhu, J. Huang, F. Jiang, Theoretical calculations and experimental verification for the pumping effect caused by the dynamic micro-tapered angle, Chinese Journal of Mechanical Engineering 29 (2016) 615–623.

[15] J. Zhang, Q. Yan, J. Huang, C. Wu, Experimental verification of the pumping effect caused by the micro-tapered hole in a piezoelectric atomizer, Sensors 18 (2018) 2311.

[16] Q. Yan, J. Zhang, J. Huang, Y. Wang, The effect of vibration characteristics on the atomization rate in a micro-tapered aperture atomizer, Sensors 18 (2018) 934.

[17] Q. Yan, W. Sun, J. Zhang, Study on the influencing factors of the atomization rate in a piezoceramic vibrating mesh atomizer, Applied Sciences 10 (2020) 2422.

[18] H. Zhou, L. Shi, J. Tan, S. Huang, The design of medical micro atomization device based on piezoelectric actuators, IOP Conference Series: Materials Science and Engineering 563 (2019) 042039.

[19] Chen, Yan, Ma, Chunyan, Shen, Zaihe, Chen, Rui, Research on vibration characteristics of piezoelectric ceramic atomizer based on ansys, E3S Web Conf. 118 (2019) 02043.

[20] E. D. Dupuis, A. M. Momen, V. K. Patel, S. Shahab, Coupling of electroelastic dynamics and direct contact ultrasonic drying formulation for annular piezoelectric bimorph transducers, Smart Materials and Structures 29 (2020) 045027.

Analytical model of the dynamic behavior of a vibrating mesh nebulizer for optimal atomization efficiency

Local scale

Kinematics of a perforation

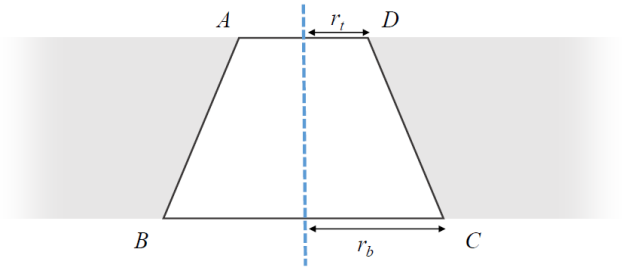

Analytical estimation of dynamic volume change in each hole according to the deflection experienced by each hole.

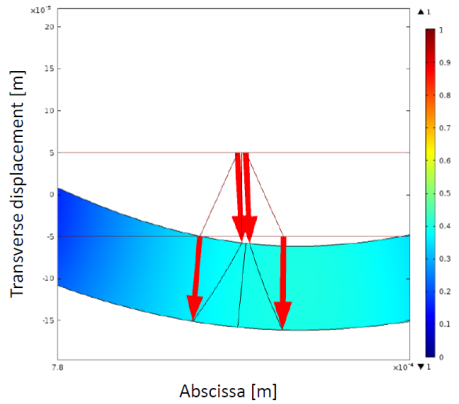

Circular perforated plate and piezoelectric ring

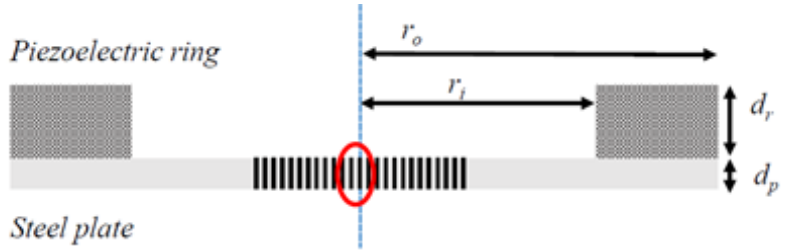

Motivation : volume change in the mesh is a key factor in atomization efficiency

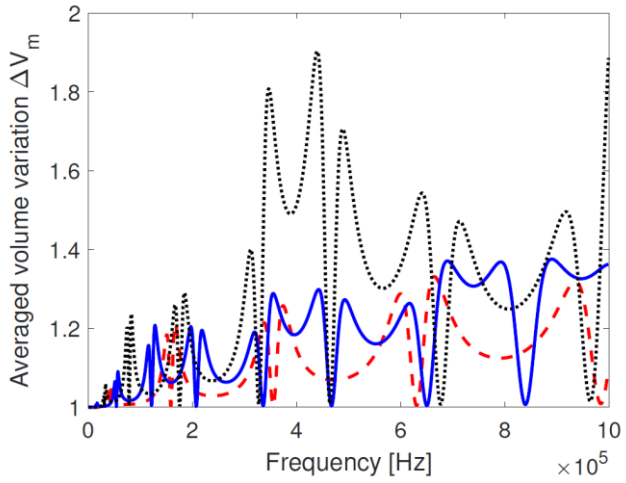

Output : Analytical model providing the dynamic volume change, suitable for parametric study and derivation of design rules.

Global scale

FEM validation of theoretical model on stepped plate

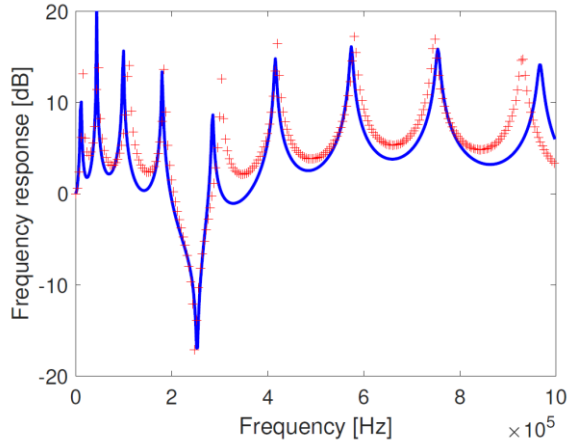

Maxima of volume change identified with respect to modal shapes